Greener, Safer and Better Performing Aqueous Binder for Positive Electrode Manufacturing of Sodium Ion Batteries

Ruochen Xu,‡[ab] Venkat Pamidi,‡*[a] Yushu Tang,[cd] Stefan Fuchs,[ae] Helge S. Stein,[ae] Bosubabu Dasari,[ac] Zhirong Zhao-Karger,[ac] Santosh Behara,[f] Yang Hu,[a] Shivam Trivedi,[a] M. Anji Reddy,[f] Prabeer Barpanda,[acg] and Maximilian Fichtner *[ac]

[a] *Helmholtz Institute Ulm (HIU), Helmholtzstraße 11, 89081 Ulm, Germany*

[b] *Technical University of Munich, Lichtenbergstraße 4, 85748 Garching, Germany*

[c] *Institute of Nanotechnology, Karlsruhe Institute of Technology, 76021 Karlsruhe, Germany*

[d] *Karlsruhe Nano Micro Facility (KNMF), Karlsruhe Institute of Technology (KIT), Eggenstein-Leopoldshafen, Germany*

[e] *Institute of Physical Chemistry (IPC), Karlsruhe Institute of Technology (KIT), Fritz-Haber Weg 2, 76131 Karlsruhe, Germany*

[f] *Faculty of Science and Engineering, Swansea University, Fabian Way, Swansea SA1 8EN, United Kingdom*

[g] *Faraday Materials Laboratory (FaMaL), Materials Research Centre, Indian Institute of Science, Bangalore 560012, India*

‡ *RX and VP contributed equally to this work.*

* Corresponding author: venkateswarlu.pamidi@uni-ulm.de

venkateshp.mme@gmail.com

Abstract

P2-type cobalt-free MnNi-based layered oxides are promising cathode materials for sodium-ion batteries (SIBs) due to their high reversible capacity and well chemical stability. However, the phase transformations during repeated (dis)charge steps lead to rapid capacity decay and deteriorated Na^+ diffusion kinetics. Moreover, the electrode manufacturing based on polyvinylidene difluoride (PVDF) binder system has been reported with severely defluorination issue as well as the energy intensive and expensive process due to the use of toxic and volatile N-methyl-2-pyrrolidone (NMP) solvent. It calls for designing a sustainable, better performing, and cost-effective binder for positive electrode manufacturing. In this work, we investigated inorganic sodium metasilicate (SMS) as a viable binder in conjunction with P2-$Na_{0.67}Mn_{0.55}Ni_{0.25}Fe_{0.1}Ti_{0.1}O_2$ (NMNFT) cathode material for

SIBs. The NMNFT-SMS electrode delivered a superior electrochemical performance compared to carboxy methylcellulose (CMC) and PVDF based electrodes with a reversible capacity of ~161 mAh/g and retaining ~83% after 200 cycles. Lower cell impedance and faster Na^+ diffusion was also observed in this binder system. Meanwhile, with the assistance of TEM technique, SMS is suggested to form a uniform and stable nanoscale layer over the cathode particle surface, protecting the particle from exfoliation/cracking due to electrolyte attack. It effectively maintained the electrode connectivity and suppressed early phase transitions during cycling as confirmed by *operando* XRD study. With these findings, SMS binder can be proposed as a powerful multifunctional binder to enable positive electrode manufacturing of SIBs and to overall reduce battery manufacturing costs.

Key words: sodium-ion batteries, layered oxide cathodes, aqueous binder, sodium metasilicate, *in-situ* coating, thermal stability.

Introduction

The cathode is a critical player determining the performance and cost of a battery.[1,2] Over the years, several types of cathode materials have been reported for sodium-ion batteries (SIBs), such as layered transition-metal oxides, polyanionic compounds, and Prussian blue analogues.[3,4] A great number of layered transition metal oxide materials (Na_xTMO_2, where TM = Mn, Ni, Fe and Ti etc.) have been studied since the report of Delmas *et al.*,[5] owing to their high theoretical capacity, low material cost and simple synthesis procedures.[1,6] Depending on the sodium environment and the stacking orders of different oxygen layers, the layered oxide materials are divided into different types such as P2 (ABBA), O2 (ABAC), P3 (ABBCCA) and O3 (ABCABC).[7] The P2 and O3 types are the most commonly reported phases, where P and O stands for prismatic and octahedral sites of Na^+ ions while the following number implies the number of TMO_2 layers in the unit cell. The P2-type materials deliver higher reversible capacity and better rate capability due to faster Na^+ mobility compared to that of O3 type structures.[8,9]

Among various reported P2-type cathode materials, the cobalt-free $Na_{2/3}Mn_{2/3}Ni_{1/3}O_2$ (NMNO) has been considered a promising candidate, which exhibits a large initial capacity with wide voltage window but suffers from poor cycling stability.[10] Lu *et al.* first demonstrated that the material undergoes a P2-O2 phase transition upon de-sodiation, within the voltage range of 2.0–4.5 V (vs. Na/Na^+), where the P2 phase starts to evolve into the O2 phase from 4.15 V. It was completely converted to O2 phase when the electrode was charged to 4.4 V.[10] In addition to the P2-O2 phase transition, an orthorhombic distorted phase called P2′ has been observed during deep discharge state.[11] Such phase transformations typically involve large volume changes, which lead to strain in the material up to the collapse of the layered structure, cracking of particles and electrical isolation of active

material, resulting in rapid capacity loss and poor cycle life. Moreover, several voltage plateaus can be observed, which are associated with the interlayer sodium/vacancy ordering resulting in a restricted Na^+ diffusion, leading to limited rate capability.[7,10] Hence, significant efforts have been geared to address these issues to improve the electrochemical performance.

Among them, electrochemically inactive elemental doping forms an effective strategy.[12,13] Wang *et al.* described a novel quaternary cathode material P2-$Na_{0.67}Mn_{0.55}Ni_{0.25}Fe_{0.1}Ti_{0.1}O_2$ (NMNFT) with a theoretical capacity of 175 mAh/g.[12] The introduction of the electrochemically inactive elements Ti and Fe into the transition metal layer (TMO_2) has proven to stabilize the structure at high cut-off voltages by suppressing the TMO_2 slabs gliding as well as the new phase formation, which effectively mitigates the cell volume changes.[12–14] The sodium/vacancy ordering induced voltage plateaus/ two-phase regions were also suppressed by partial substitution of Mn^{3+} by Ti^{4+}. This was accompanied by a smooth charge/discharge curve with pure solid-solution reaction during sodium intercalation and deintercalation.[15] Additionally, partial substitution of Ni with Fe reduced the high demand of expensive nickel oxide, but maintained the high working voltage of the cell along with good chemical stability against humidity.[16,17]Additionally, surface modification[18] and utilization of aqueous binders[19,20] have also been reported as effective strategies to improve electrochemical performance.

Binders account for only 2–5% of the total weight of an electrode but play an important role to enable flexible fabrication of the electrode by binding the active materials and conductive carbon together, and to the current collector. Owing to the high chemical and electrochemical stability in the wide voltage window, the organic binder polyvinylidene difluoride (PVDF) and its derivates have been commonly employed for electrode processing.[19,20] To dissolute this binder, *N*-methyl-*2*-pyrrolidone (NMP) solvent is widely used, even though it has a high boiling point of 202 °C and is toxic.[20,21] As a consequence, energy intensive and expensive solvent evaporation and recovery processes are required. Liu *et al.* pointed out that coating/drying/recovery process is the most cost intensive (up to 20% of total manufacturing cost) and energy intensive (46.8% of total energy consumption) process in the battery manufacturing.[22] Therefore, there is still an urgent need for multifunctional, sustainable, and aqueous binders to meet the actual requirements.

In this context, low-cost, environment friendly, and ionically conducting aqueous-based binders have been considered as a promising alternative.[23] Carboxy methylcellulose sodium salt (CMC), a linear polymer from natural cellulose, has been extensively studied as a binder for negative electrode materials and sparsely investigated for positive electrode materials in SIBs. Owing to its good binding strength and ion-conductive network, electrodes with CMC exhibit superior electrochemical performance compared to PVDF.[23,24] Nonetheless, some serious problems such as corrosion of current collector,[25,26] low thermal stability,[27] and low elastomeric

properties[28] were reported with CMC. Recently, sodium-based phosphates and silicates have also been reported by our group[29–31] and others[32] as potential multifunctional binders for SIBs due to their excellent thermal stability, ionic conductivity and high binding ability. Jiao *et al*.[18] reported the surface coating of sodium polysilicate on cathode material surface, which effectively inhibited the side reactions and ensured the Na^+ diffusion during cycling. However, the number of publications related to aqueous binders for positive electrode manufacturing is still marginal, mostly because current cathode materials are not stable in water/moisture-based processes (see **Table S1**). This necessitates the development of water/moisture stable cathodes in conjunction with multifunctional aqueous binders.

In this study, sodium metasilicate (SMS) was employed as a binder for model P2-type $Na_{0.67}Mn_{0.55}Ni_{0.25}Fe_{0.1}Ti_{0.1}O_2$ (NMNFT) cathode material. Its physico-chemical, electrochemical, and thermal properties were compared with CMC- and PVDF binder-based electrodes. It was found that both aqueous binder-based electrodes perform much better as compared to PVDF based electrode with respect to their electrochemical and thermal properties. In addition, transmission electron microscopy and X-ray photoelectron spectroscopy of pristine and cycled electrodes revealed that SMS forms a passive layer over the active material effectively suppressing the side reactions between active material and electrolyte leading to improved cycling stability. Owing to this *in-situ* surface modification, no phase transition was observed for SMS-based electrode during electrochemical cycling as confirmed by *operando* XRD. Additionally, accompanied with an excellent binding ability, SMS electrode delivered a high-capacity retention and rate capability compared to CMC and PVDF-based electrodes.

Experimental section

Material synthesis

P2-type $Na_{0.67}Mn_{0.55}Ni_{0.25}Fe_{0.1}Ti_{0.1}O_2$ (NMNFT) was synthesized via solid-state reaction. Stoichiometric amounts of Na_2CO_3 (98%, Alfa Aesar), Mn_2O_3 (98%, Alfa Aesar), NiO (99%, Alfa Aesar), Fe_2O_3 (99.9%, Alfa Aesar), and TiO_2 (≥99.9%, VWR chemicals) were intimately mixed by ball-milling (500 rpm for 2 h) at room temperature in air. Subsequently, the resultant mixture was calcined at 900 °C for 15 h in a muffle furnace with a heating rate of 5 °C/min. After calcination, the material was slowly cooled down to 100 °C (5 °C min^{-1}) and was transferred into an argon-filled glovebox to avoid further contact with humidity from ambient atmosphere. All the chemicals were used as received.

Physico-chemical characterization

The phase analysis of the samples was performed using an X-ray diffractometer (STOE-Stadi P) equipped with a Mo Kα radiation source (50 kV/40 mA) in the transmission mode. *Operando* XRD measurements were carried out on different binder electrodes to gain insight into the crystal structure changes and possible phase transitions during the initial two charge-discharge cycles at a rate of 0.1C within the potential window of 4.2–1.5 V. *Operando* measurements were carried out on the same diffractometer with an Ag Kα radiation source (40 kV/40 mA) in 2θ range of 3–25°. CR2023 type coin cells with a glass window were assembled and cycled using a single channel potentiostat (Biologic SP-150). Rietveld refinement was performed on selected data using FullProf software.[31]

Microstructural investigation was carried out by scanning electron microscopy coupled with energy dispersive X-ray spectroscopy (SEM-EDX) (Thermo Scientific Apreo 2 SEM). The particle size distribution of pristine cathode material was measured by laser diffraction particle size analyser (Mastersizer 3000, Malvern Panalytical) with isopropanol as dispersant. Transmission electron microscopy (TEM) analysis was carried out using a probe aberration corrected Themis 300 (ThermoFischer Scientific) operated at 300 kV. The TEM images and selected area electron diffraction (SAED) patterns were acquired by a Ceta CCD camera (ThermoFischer Scientific). The EDS maps were obtained via a high-angle annular dark field (HAADF) detector (Fischione) and a Super-X EDX detector (ThermoFischer Scientific).

Transmission X-ray absorption spectroscopy (XAS) was performed using a laboratory device (easy XAFS 300+, easy XAFS LLC) to determine the material bulk electronic structure. Mn, Ni, Fe and Ti *K*-edge absorption spectra were collected on cellulose-diluted powder samples and compared with reference standards with known oxidation state. X-ray photoelectron spectroscopy (XPS, Specs Enviro ESCA) was employed to investigate the oxidation states of transition metals as well as to find out the surface composition of pristine and cycled electrodes. The XPS measurements were performed using a monochromatic Al Kα source (1486.71 eV). Survey spectra and high-resolution spectra were taken at 100 eV and 30 eV pass energies, respectively. The resulting data were analyzed with CasaXPS software using a Shirley type background and Gaussian (70%)-Lorentzian (30%) profiles.[32] All cycled electrodes were washed with dimethyl carbonate (DMC, Sigma Aldrich) and were dried at 50 °C for 1 h in a glove box before further characterization.

Thermogravimetric analysis coupled with differential scanning calorimetry (TGA-DSC, Setaram thermal analyzer SENSYS evo instrument) measurements were carried out on charged electrodes made of different binders, from 30 °C to 600 °C with a ramp rate of 5 °C/min. The powder was scratched off the aluminum current collector and was filled in an alumina crucible for TGA-DSC measurements.

Electrochemical testing

Polyvinylidene difluoride (PVDF, Kynar HSV 900), carboxy methylcellulose sodium salt (CMC, Sigma Aldrich) and sodium metasilicate (SMS, Sigma Aldrich) were used as binders. A homogeneous slurry was prepared by mixing 80 wt.% of active material, 10 wt.% of conductive carbon black (Super C65, C-NERGY), and 10 wt.% of binder dispersed in *N*-methyl-*2*-pyrrolidone (NMP, 99.5%, Alfa Aesar) solvent for PVDF and deionized water (Milli-Q® Water Purification System) solvent for CMC and SMS binders. The obtained slurry was mixed at 2000 rpm for 20 minutes with a high-speed mixer (Thinky, ARE-250) and was cast on Al foil for PVDF binder or on carbon coated Al foil for aqueous binders with a doctor blade coater. After drying at 110 °C for 12 h in vacuum, the coated electrodes were pressed with a calendaring machine (MTI Corporation, OT Rolling press) to approximately 50% of its initial thickness to minimize the porosity. These calendared electrodes were transferred into a glove box and punched into 12 mm discs for cell fabrication. The mass loading of the active material was ~4 mg/cm^2 (average of 10 electrodes each). CR 2032 coin-type half cells were assembled in a glove box using Na metal as anode and borosilicate glass fiber sheet as separator. The electrolyte consisted of 1M sodium perchlorate ($NaClO_4$) in a mixture of propylene carbonate (PC)/ fluoroethylene carbonate (FEC) (98/2, v/v). Hard carbon[33] (~1 mg mass loading) anode was prepared in a similar manner to the cathode with 80 wt.% of hard carbon, 10 wt.% of conducting agent and 10 wt.% CMC to assemble a full cell. The cells were cycled at room temperature using a Biologic BCS-805 battery cycler. Before each test, the cell was rested for 7 h to reach a steady state. Cyclic voltammetry (CV) was carried out with a scan rate of 0.1 mV/s. Electrochemical impedance spectroscopy (EIS) measurements were performed in a frequency range of 10 kHz-10 mHz with an AC amplitude of 10 mV. Galvanostatic intermittent titration technique (GITT) was used to determine the chemical diffusion coefficient. For the GITT test, the cells were galvanostatically (dis)charged at a current rate of 0.1C for 15 mins, then the applied current was cut off and held for 90 mins to allow the full diffusion of Na^+ within the active material to reach an equilibrium state.

Result and discussions

Physico-chemical characterizations

P2-type $Na_{0.67}Mn_{0.55}Ni_{0.25}Fe_{0.1}Ti_{0.1}O_2$ (NMNFT) was synthesized by solid-state method. Inductively coupled plasma optical emission spectroscopy (ICP-OES) determined a composition of $Na_{0.60}Mn_{0.54}Ni_{0.25}Fe_{0.09}Ti_{0.09}O_2$ that was in good accordance with the target composition, despite some sodium loss during the calcination. **Figure S1a** shows the Rietveld refined XRD pattern of pristine NMNFT cathode

material with the lattice parameters: $a = b = 2.902(4)$ Å and $c = 11.191(3)$ Å. All the diffraction peaks were well indexed with the parent $Na_{0.7}MnO_{2.05}$ with a typical layered hexagonal structure with a space group of *P*63/*mmc* (ICSD file: 00-027-0751) accompanied with the fitness parameter of $\chi^2 = 3.71$. A schematic illustration of the crystal structure is shown (see inset in **Figure S1a**). The corresponding crystallographic data are summarized in **Table S2**. The pristine cathode material showed an irregularly shaped secondary particles consisting of a large number of smooth, plate shaped primary particles (**Figure S1b**). An average secondary particle size (D_{50}) of 16 µm was observed from laser particle analyser. However, the poor chemical stability of the layered oxide cathode materials under humid conditions is one of the key issues hindering its large-scale implementation. In order to test the bulk chemical-stability, air and water aging tests were performed on the pristine NMNFT cathode material (60 days air exposure and 1h stirring in water). The particle morphology as well as the crystal structure were evaluated by SEM and XRD, respectively. It was found that NMNFT cathode material exhibited robust bulk chemical stability against air/water exposure. No distinct differences have been found from XRD patterns (**Figure S1c, 1d**) as well as the particle morphology (see **Figure S1e, 1f**) after these tests.

Subsequently, the average oxidation state of the transition metals in the bulk material was characterized by XAS. **Figure S2** shows the normalized XANES (X-ray absorption near edge structure) spectra. The respective metal K-edges were evaluated by "fingerprint" method with several known standards. It was found that the edge energy position of Mn and Ni was close to that of MnO_2 and $NiO/Ni(OH)_2$, respectively, indicating an average Mn^{4+} and Ni^{2+} oxidation states. Meanwhile, Fe and Ti were found to be in Fe^{3+} and Ti^{4+} oxidation states. Since the novelty of this paper is not on cathode material itself but more on the different binder-cathode system, more results would be given with different binder-based electrodes. Therefore, surface analysis of pristine electrodes based on different binder systems was carried out using X-ray photoelectron spectroscopy (**Figure 1**). The Mn^{4+}, Ni^{2+} and Ti^{4+} are observed in the corresponding Mn 2*p*, Ni 2*p* and Ti 2*p* spectra (see **Figure 1a, 1b, 1c**) of all electrodes, respectively. These are in good agreement with XANES results (see **Figure S2**), indicating a homogeneous structure of the cathode from the bulk to surface. However, the Fe^{4+} are hardly detected by XPS and can be attributed to the surface inhomogeneities. Additionally, as shown in **Figure S3a,3b**, several peaks are observed for at 1072 eV (Na *1s*) and 529.5 eV, 531.4 eV and 532.7 eV (O *1s*) regions for all binder-based electrodes, respectively. Nevertheless, increased in the binding energy shifts for Na and O signals has been observed for CMC based electrode, which could be related to the different chemical environment present as a result of CMC interaction with NMNFT cathode material.[34,35]

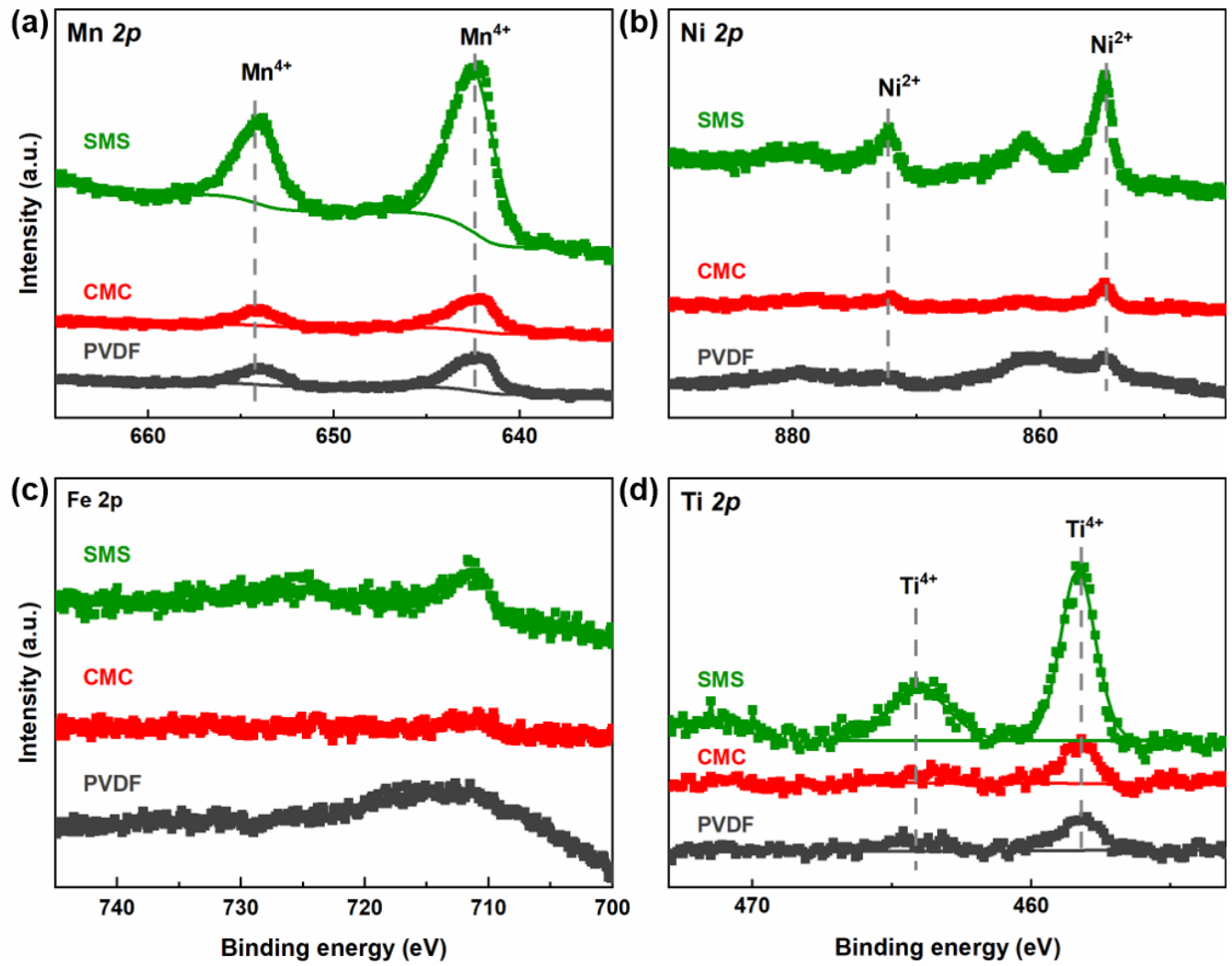

Figure 1. XPS profiles of (a) Mn 2p, (b) Ni 2p, (c) Fe 2p and (d) Ti 2p regions recorded from different pristine MNMFT-binder based electrodes.

To verify the influence of binder on cathode performance, it is necessary to understand the binding mechanisms. The binding ability of PVDF is mainly achieved by a physico-mechanical interlocking, which is relatively weak compared to the chemical bonds formed between CMC and active material.[34] Meanwhile, SMS exhibits higher binding strength via condensation reaction of its OH^- groups with surface functional groups of electrode materials. This condensation mechanism has been reported elsewhere.[29] For instance, lithium polysilicate was reported as a potential binder for Si anode. It first gets hydrated during aqueous processing and then reacts with hydroxyl groups present on surface of Si via condensation reaction to form Si-O-Si bonds and thus leading to good adhesion.[29] For a better understanding, the binder distribution in the electrode is schematically illustrated in **Figure S3a**.[36] In general, the binder with higher binding ability is considered to effectively restrain the detachment of electrode composites and maintain the electrode integrity during cell cycling.[34] Inspired by Zhao *et al*.,[23] binding strength of three employed binders was measured via a peel-test

experiment as shown in **Figure S3b**. It is found that both aqueous binders displayed higher binding strength than that of PVDF binder (SMS-9.0 N, CMC-4.2 N and PVDF-1.6 N). Especially, SMS binder exhibited the highest value of 9.0 N, which is almost twice that of CMC and over five times that of PVDF and may explain the superior electrochemical performance as shown in next sections.

A typical low magnification transmission electron microscopy (TEM) images of the pristine NMNFT-SMS-based electrodes (shown in **Figure 2a**) was performed, as it was anticipated that SMS forms an in-situ coating layer on the cathode and carbon particles. Atomic-resolution HAADF image in **Figure 2b** confirms a high crystallinity of active material with an interlayer distance of 0.563 nm for (002) crystal plane. Additionally, dotted ring diffraction patterns (**Figure 2c)** as well as diffused ring patterns (**Figure 2d**) demonstrate the polycrystalline nature of NMNFT cathode material and binder/carbon mixture, respectively. From the EDS mappings in **Figure 2e** and the corresponding spectra in **Figure S5**, all elements were found to be uniformly distributed. It's worth noting that Si signal corresponding to SMS binder uniformly covered on the cathode and carbon surface and it suggests for the formation of nanoscale layer over the particle surface.

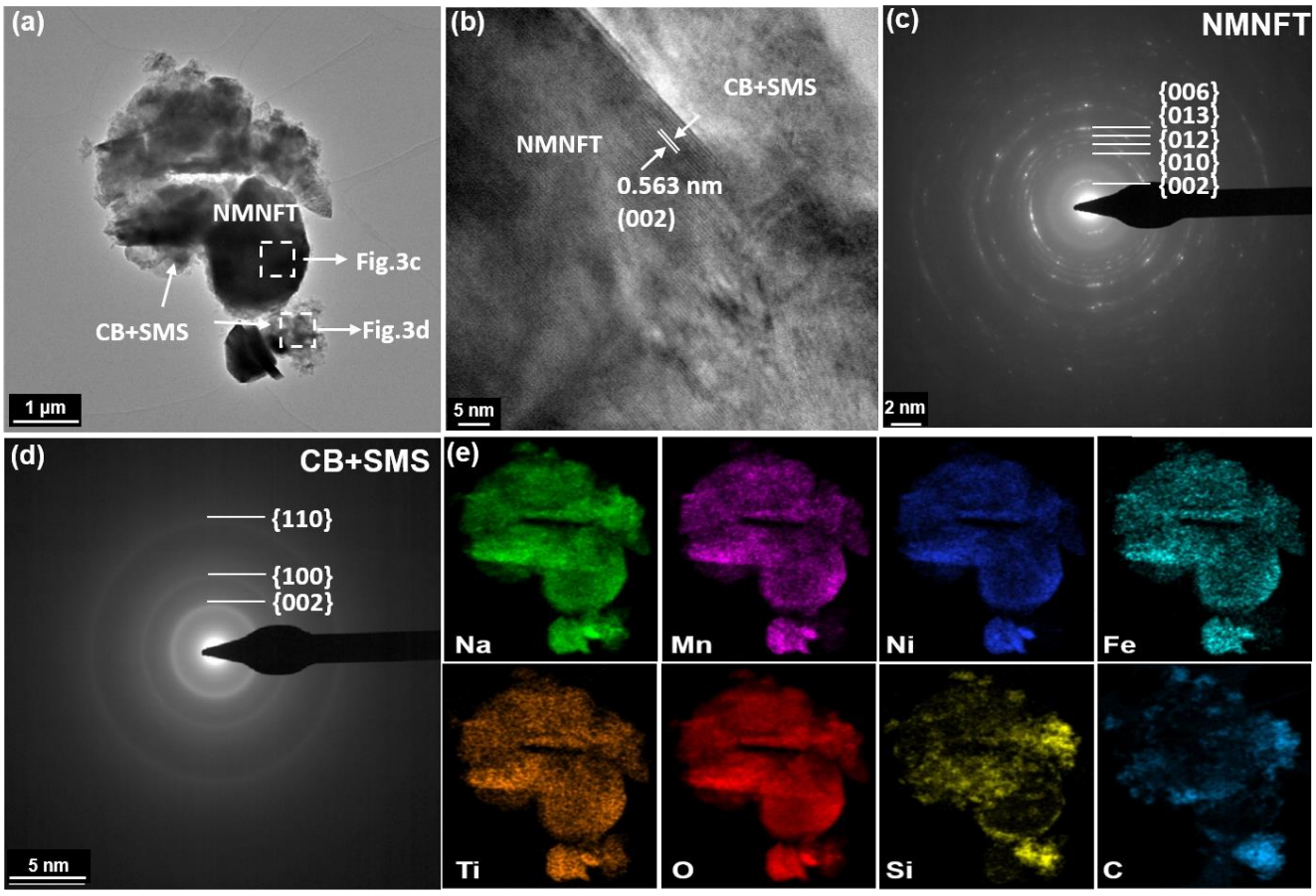

Figure 2. TEM analysis of NMNFT-SMS-C pristine electrode. (a) Overview bright-field TEM image; (b) corresponding HRTEM image; SAED patterns of (c) active material and (d) SMS/Carbon black mixture; (e) STEM-EDS mapping of Na, Mn, Ni, Fe, Ti, O, Si and C elements.

Scanning electron microscopy (SEM) was employed on all binder-based electrodes to further investigate the effect of binders on the electrode coating quality (see **Figure S6**). It was found that all electrodes except for pure CMC-based electrode (**Figure S6b**) show smooth surface. It's worth mentioning that similar behavior has been reported for CMC binder with other layered oxide cathode materials for SIB[26] and were attributed to the preferential absorption of CMC on the electrode components rather than the current collector. It can lead to cracks and cavities in the electrodes, which adversely affect the electronic conduction and thereby poor cycling performance, especially at high C-rates.[26,37] To avoid this, a direct slurry pH control strategy with phosphorous acid (PA) addition was reported in LIBs research and therefore also applied in our studies. It was found that the pH modified CMC/1wt.% PA electrode exhibited a significantly improved coating quality without any cavity formation (see **Figure S4c**). However, in case of pure SMS based electrode show already a relatively smooth surface, the pH modification with PA barely help to improve the coating quality, **as shown in Figure S6d, 5e**.

Electrochemical performance evaluation

The electrochemical performance of binder-based NMNFT electrodes (PVDF, CMC and SMS) was evaluated in half cells against sodium metal anode using CR2032-type coin cells. Firstly, cyclic voltammetry (CV) was carried out with a scan rate of 0.1 mV/s between 4.2–1.5 V. As shown in **Figure S7a-c**, three redox pairs were observed at 2.1 V/1.8 V, 3.5 V/3.4 V and 3.6 V/3.5 V. They correspond to the $Mn^{3+/4+}$ redox pair (at low potential) and $Ni^{2+/3+/4+}$ redox pairs (at high potential), respectively. The constituent Ti and Fe were found to be electrochemically inactive and act solely as structure stabilizers.[12] It's worth mentioning that the potential gap between the redox pairs could effectively infer the reversibility of redox reaction as well as the material structure stability. In this work, the potential gap for Mn redox was defined as E_a, while E_b represents the potential gap for Ni redox pairs. Notably, the PVDF based electrode exhibited the largest potential gap on both Mn and Ni redox pairs during the initial five cycles, compared to aqueous binder-based electrodes (see **Table S3**). This demonstrates that the irreversibility of Mn and Ni redox reactions increased during cell cycling, which could be assigned to the side reactions between active material and electrolyte. Considering the ICP-OES result and the oxidation states, the total cation charge for this cathode is 3.89, which is lower than anion charge. This suggests that the sample might have oxygen vacancies. Such oxygen vacancies can have detrimental effect on the cycling stability due to the associated oxygen loss (irreversible oxygen redox) from the cathode particle surface and the potential irreversible phase transformations or particle cracking. These irreversible reactions can be significant in

PVDF electrode due its poor binding strength. In contrast, CMC and SMS electrodes exhibited well overlapped profiles and had lower E_a and E_b values, indicating improved redox activities of Mn and Ni pairs. Furthermore, similar results were obtained from the charge-discharge profiles of these electrodes for initial five cycles at a rate of 0.1C between 4.2–1.5 V (see **Figure S7d-f**). The first charge capacities were 90, 84 and 93 mAh/g for PVDF, CMC and SMS based electrodes, respectively, and the lower first charge capacities are due to the Na-deficiency in P2-type compounds. In the case of PVDF-electrode, there is a noticeable drop in the discharge capacities and increased ohmic polarization during cycling. However, both aqueous binder-based electrodes exhibited well overlapped charge-discharge profiles, suggesting a good structural stability and thereby improved reversibility during cycling. [17]

Figure 3a displays the 2nd charge-discharge profiles with reversible discharge capacities of 167.3, 152.7, 159.6 and 161.5 mAh/g for PVDF, CMC, CMC-PA and SMS electrodes, respectively. Among them, all aqueous binder electrodes exhibited slightly lower reversible capacities compared to that of PVDF-based electrode, which is attributed to the loss of Na^+ or proton exchange as a result of water processing.[17] A detailed investigation was carried out to understand the effect of aging (air exposure for 60 days and water stirring for 1h) of cathode material on the electrochemical performance. In short, no significant drop in capacity was observed for water stirred sample although the air exposed sample exhibited deteriorated performance possibly due to the depletion of Na^+ from the cathode particle surface. The results are presented in **Figure S8** and **Table S4**.

Afterwards, the cycling stability of these electrodes was evaluated at 0.2C and 1C rates in the potential window 4.2–1.5 V as shown in **Figure 3b, 3c**. Among them, SMS based electrode exhibited a reversible capacity of ~161 mAh/g with a capacity retention of 86.7% after 100 cycles at 0.2C and 83.3% after 200 cycles at 1C. In contrast, PVDF based electrode delivered the highest initial capacity of 167.5 mAh/g but retained only 80.2% after 100 cycles at 0.2C and 66.2% after 200 cycles at 1C. The capacity fading (more prevalent at higher rates) for PVDF based electrode could be related to electrode exfoliation associated with electrolyte penetration into the bulk structure, which also caused the transition metal degradation/dissolution and occurrence of phase transitions.[38] To confirm the occurrence of phase transitions and the possible transition metal degradation/degradation, XPS studies of cycled electrodes and *operando* XRD measurements were carried out, which will be discussed in latter sections. For unmodified CMC electrode, good cycling stability was observed at low rate (0.2C) with 88.9% capacity retention after 100 cycles. However, when the C-rate was increased to 1C, the capacity retention drastically dropped to 55.5% after 200 cycles. This is even lower than that of PVDF electrode, which is attributed to crack and cavity formations resulted in the electrical isolation. Meanwhile, pH modified CMC electrode showed a reversible capacity of 159.3 mAh/g (~10 mAh/g higher than that of pure CMC electrode) and better capacity retention of 88.3% after 100 cycles at 0.2C and 70.9% after 200 cycles at 1C. This

confirms the beneficial effect of PA to enhance the electrochemical performance by improving the electrode coating quality. Nevertheless, as mentioned previously, no significant improvement has been observed for SMS based electrode with PA addition, where it showed a comparable reversible capacity of 160.5 mAh/g with a capacity retention of only 76.7% after 200 cycles at 1C **(**see **Figure S9)**.

The rate capabilities of the above-mentioned electrodes were verified with a series of rates from 0.1C to 2C as shown in **Figure 3d**. Among them, all CMC and SMS electrodes exhibited reversible capacities of 98.3 and 100.0 mAh/g at 2C, respectively, corresponding to 65.6% and 63.5% of the initial capacity at 0.1C. However, only 83 mAh/g (corresponding to 50.3%) of the initial capacity was observed for PVDF electrode. This superior rate capability of aqueous binder electrodes was assigned to the formation robust electrode structure and highly distributed and interconnected electronic/ionic percolation network as result of higher binding ability and intrinsic ionic conductivity of aqueous binders. **Table S5 and S6** summarizes the electrochemical performance data from the cycling stability and rate tests. Owing to the superior performance in Na half-cell, the NMNFT-SMS based electrode was assembled with hard carbon anode to form a full cell. **Figure 3e** displays the initial two charge-discharge profiles of NMNFT-SMS/hard carbon-CMC full cell between 4.2–1.5 V at 0.1C. After 200 cycles at 0.5C, a capacity retention of ~77.3% was obtained (see **Figure 3f**).

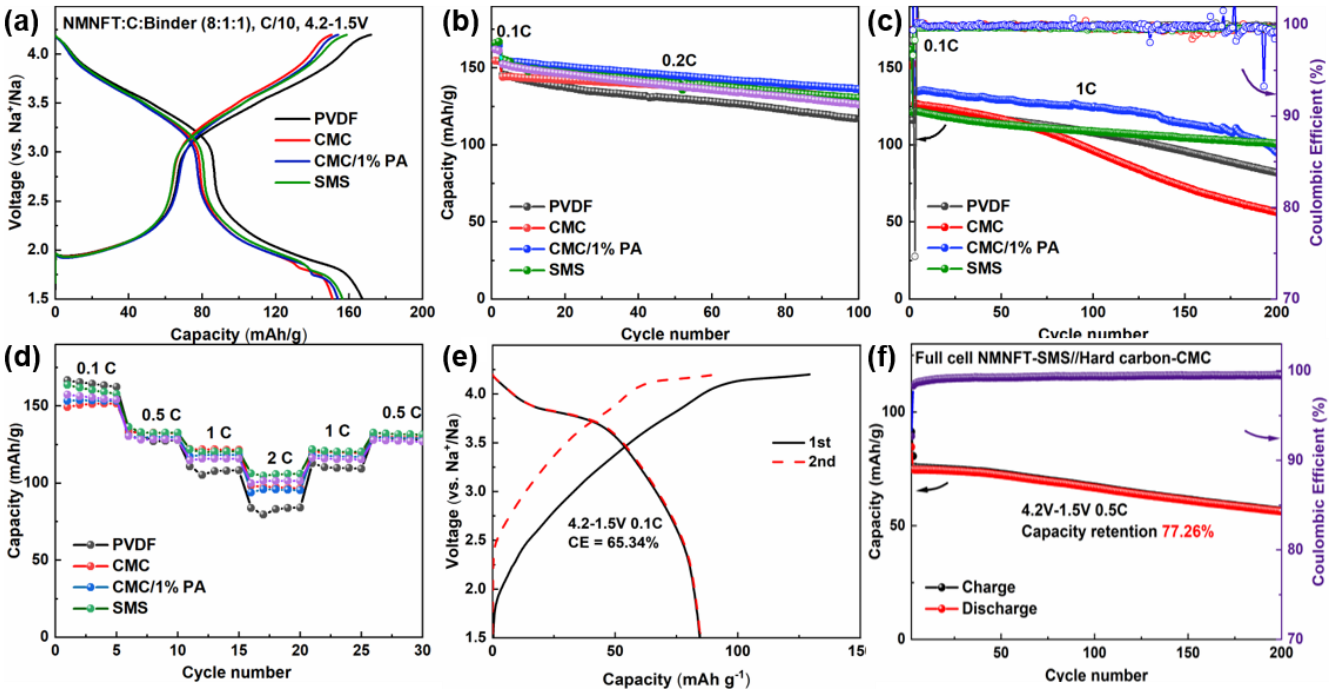

Figure 3. Electrochemical performance of NMNFT-binder electrodes in sodium half-cell between 4.2–1.5 V. (a)2nd charge-discharge profiles; (b, c) cycling performance at 0.2C and 1C rates and (d) rate performance, respectively. Electrochemical performance of NMNFT-SMS/hard carbon-CMC full cell between 4.2–1.5 V, (e) charge-discharge profiles of initial two cycles; (f) cycling performance at 0.5C.

Electrochemical impedance spectroscopy (EIS) and galvanostatic intermittent titration techniques (GITT) were used to investigate the reasons for improved rate capability and reduced polarization exhibited in CMC and SMS based electrodes. **Figure 4** and **Figure S10** display the Nyquist plots and corresponding Bode plots, respectively, of the three binder-based electrodes between 5–200 cycles at different intervals within the voltage range of 4.2–1.5 V at 1C. As shown in **Figure 4a-c**, the Nyquist plots consisted of two semicircles and a straight line. The intercept at the high frequency region corresponds to the ohmic resistance (R_e), while the semicircles at medium-high frequency region (first semicircle) and medium frequency region (second semicircle) correspond to the interfacial resistance (R_{SEI}) and charge transfer resistance (R_{ct}), respectively. The inclined line at the end of the profile is related to the Warburg impedance W. The impedance values obtained after fitting are summarized in **Figure 4d** for better understanding. Overall, PVDF based electrode exhibited higher R_{SEI} and R_{ct} values compared to that of CMC and SMS based electrodes, after the respective cycles. It's worth noting that SMS-based electrode exhibited less and decreasing interfacial resistance during cycling, because surface coverage effectively protects the active material from electrolyte attack. Nevertheless, charge transfer resistance of all the three electrodes were observed to increase, which could be due to the deteriorated Na^+ diffusion during cycling.[39,40] Additionally, only one semicircle was observed for CMC electrode after 100 cycles, which was generally obtained from thin layer electrodes.[41,42] To the best of our knowledge, so far, no reasonable explanation was found for this behavior. In short, SMS electrode exhibited the lowest impedance among these electrodes including the R_e, R_{SEI} and R_{ct} impedances, demonstrating that SMS binder can greatly improve the surface conductivity (due to the intrinsic ionic conductivity of SMS) and facilitate the faster Na^+ diffusion during cycling. Moreover, the surface coverage also helps to avoid electrolyte decomposition on the active material surface and reduce the cathode polarization.

Figure 4e displays the Warburg plots of Z' vs. $\omega^{-1/2}$ at low frequency region, in which the slope corresponded to the Warburg coefficient σ. The Na^+ diffusion coefficients D_{Na+} for corresponding electrodes were calculated with reference to Wang *et al*.[43]

$$D = \frac{R^2T^2}{2A^2n^4F^4c^2\sigma^2} \quad (1)$$

where R is the gas constant (8.314 J K^{-1} *mol^{-1}), T is the room temperature (298.15 K), A is the electrode surface area (1.131 cm^2), n is the number of electrons transferred per molecules during cycling (0.67), F is the Faraday constant (96485 C*mol^{-1}), c is the concentration of Na^+ in the NMNFT electrodes (1.242×10^4 mol*m^{-3}) and σ is the Warburg constant recorded in Warburg plots. A summary of the applied parameters for calculating the D_{Na+} from EIS was presented in **Table S7**. It was found that SMS electrode obtained the highest sodium diffusion

coefficient D_{Na+} value of 5.30 × 10^{-12} cm^2 s^{-1} after 200 cycles, which was higher than that in CMC electrode at 3.44 × 10^{-12} cm^2 s^{-1} and PVDF electrode at 1.78 × 10^{-12} cm^2 s^{-1}. However, these values calculated from the EIS measurements due to its "static" nature represent only an apparent sodium diffusion coefficient and cannot dynamically reflect the change of diffusion coefficient during cycling.

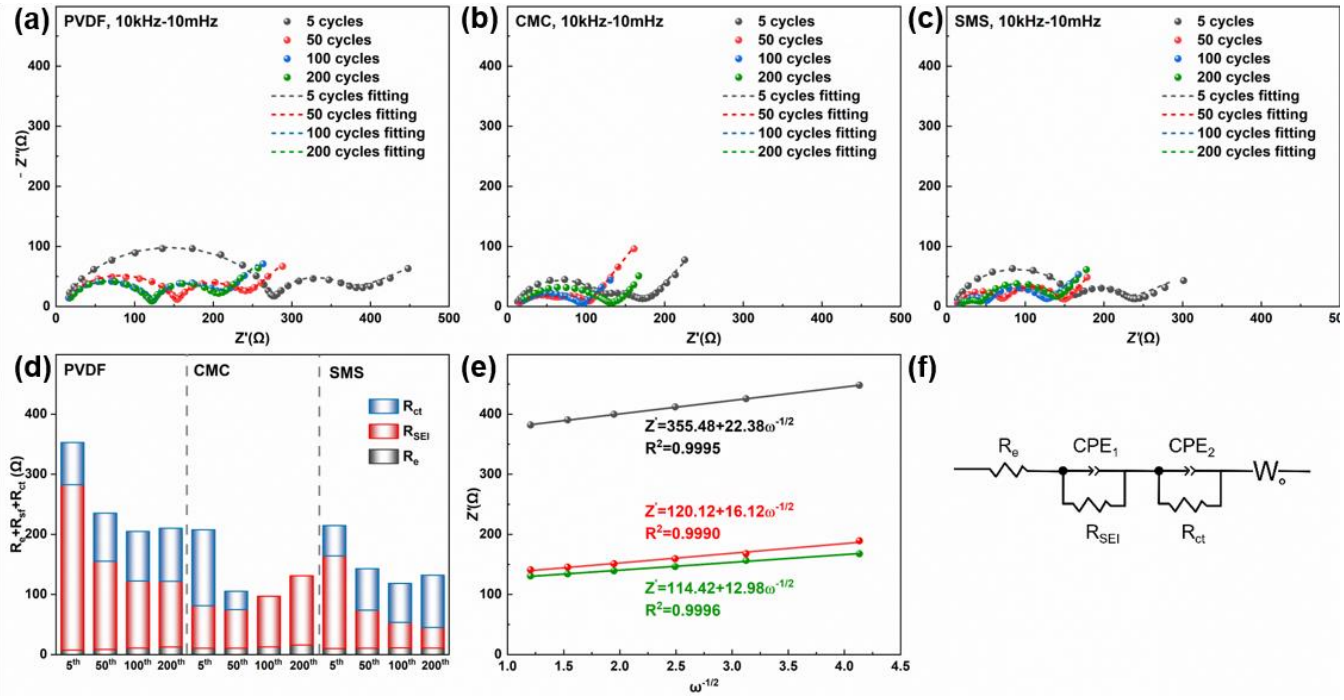

Figure 4. Nyquist plots of NMNFT-(a) PVDF, (b) CMC and (c) SMS based electrodes. The impedance data was measured after certain cycles at a rate of 1C; (d) Comparison of total impedance for all the electrodes; (e) Warburg plots of $Z^{'}$ vs. $\omega^{-1/2}$; (f) applied equivalent circuit (fitted by Z View 2.0 software). Sample codes in (e): black-PVDF, red-CMC and green-SMS.

Therefore, GITT was conducted to gain insight into Na^+ diffusion kinetics during cycling. A series of D_{Na+} values were calculated during cycling by the following equation, introduced by Weppner and Huggins.[44]

$$D = \frac{4}{\pi\tau}\left(\frac{mV_m}{MS}\right)^2\left(\frac{\Delta E_S}{\Delta E_t}\right)^2, \text{ with } \left(\tau \ll \frac{L^2}{D}\right) \quad (2)$$

Where τ is the current pulse duration (s), m is the active material weight (g), V_m is the molar volume (m^3 mol^{-1}), M is the molar weight (g mol^{-1}), s is the contact area of electrode/electrolyte (m^2), ΔE_S is the voltage variation in the steady-state and ΔE_t is related to the total voltage variation per current step and L is the electrode thickness (m). A summary of the applied parameters for calculating the D_{Na+} from GITT was presented in **Table S8**. **Figure 5a** displays the schematic illustration of a current step unit during charging process, where ΔE_S and ΔE_t represent the voltage variation in the steady-state and the total voltage variation per current step, respectively. **Figure 5b** displays the GITT voltage profiles of NMNFT-binder electrodes for 2nd cycle between 4.2–1.5 V at 0.1C. The

corresponding sodium-ion diffusion coefficients (D_{Na+}) were plotted as a function of voltage during charging and discharging in **Figure 5c, 5d** respectively. Compared to the PVDF based electrode, both aqueous binder-based electrodes exhibited faster Na^+ diffusion during charge and discharge states with values of ~10^{-10} cm^2 s^{-1}. It is worth mentioning that the diffusion coefficient was observed to drop rapidly for all the electrodes at deep charge state (~4.2 V), which could be related to the hindered the Na^+ diffusion due to the structural instabilities (slab gliding or phase transformations etc.).[11] Similarly, the diffusion coefficient began to drop for both CMC and PVDF based electrodes at deep discharge state (< 2 V), which suggests the occurrence of phase transition (P2′) as confirmed by *operando* XRD in the latter sections. In contrast, SMS electrode provided much faster Na^+ diffusion at the same region, indicating the improved Na^+ diffusion kinetics due to suppressed/delayed P2′ phase transition. Considering the lower impedance and faster Na^+ diffusion observed in EIS and GITT profiles, it can be concluded that SMS can effectively maintain the electrode integrity thereby electron/Na^+ diffusion during cell cycling.

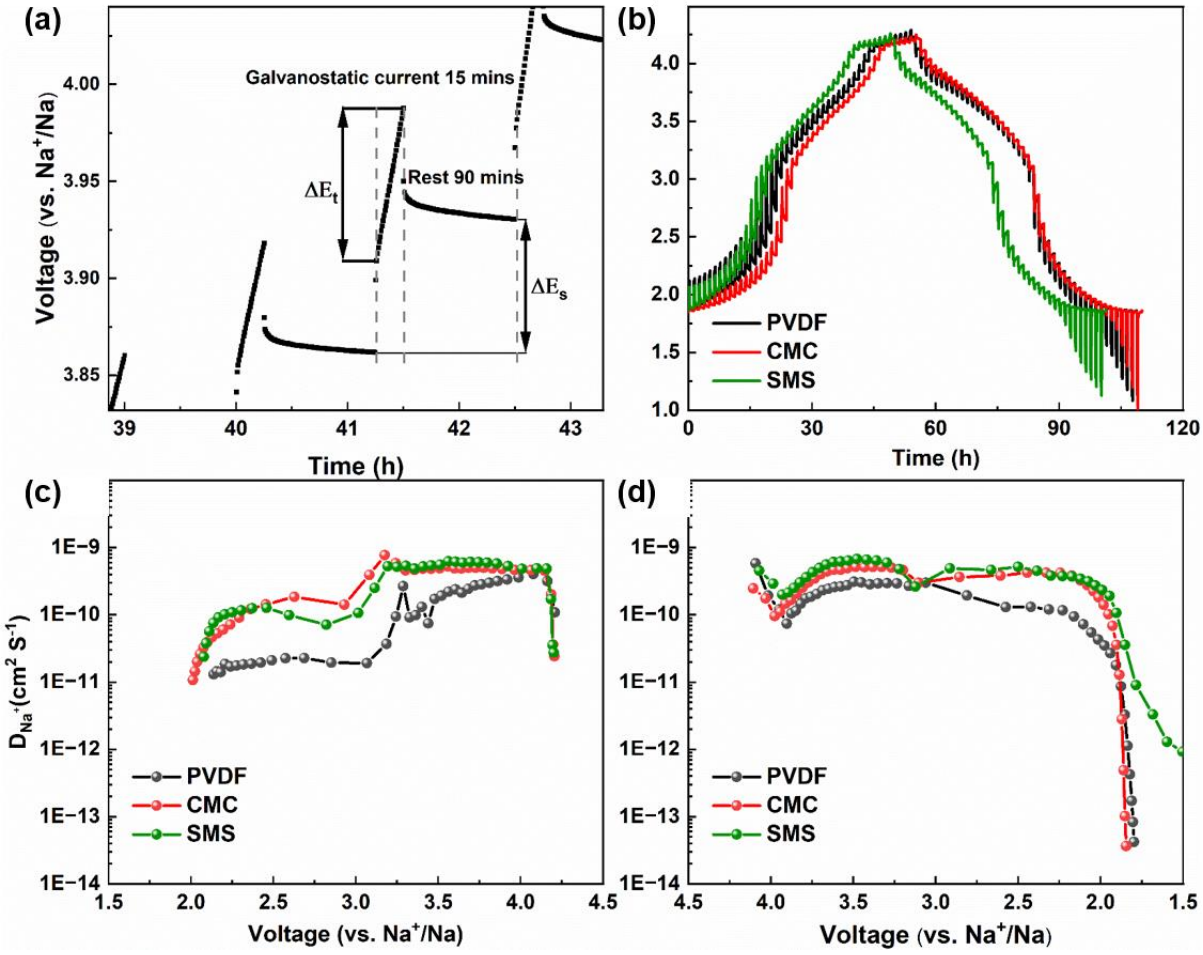

Figure 5. (a) A schematic illustration of a unit current pulse during charging process; (b) GITT voltage profiles for PVDF, CMC and SMS based electrodes; the corresponding D_{Na+} as a function of voltage for all the electrodes during (c) charging and (d) discharging processes.

Structural evolution during charge-discharge cycling

Figure S11 shows the XRD patterns of all binder-based electrodes before and after cycling. As expected, the binders did not have any impact on the crystal structure of active material. Furthermore, *operando* XRD was used to investigate the crystal structure evolution during the initial two charge-discharge cycles of the three different electrodes (see **Figure 6**). When the electrodes were charged to 4.2V, the (002) and (004) reflections for all the electrodes were found to shift towards lower 2θ angle, indicating the expansion of c-axis in the crystal structure due to the sodium extraction. Meanwhile, rest of the peaks shifted to higher 2θ angle, indicating the contraction of the respective planes. As expected, no P2-O2 phase transition was observed for all the electrodes when charged to 4.2 V owing to structure stabilization provided by Fe and Ti elemental doping.[15] While discharging, the exactly opposite phenomena occurred. The (002) and (004) reflections shifted back towards higher 2θ angle region due to the sodium insertion. This periodic peak evolution was observed for the second cycle as well for all the three electrodes, which demonstrates the reversibility of the structural changes. However, a new peak next to (002) peak was observed for both PVDF and CMC based electrodes during the deep discharge region at ~2.0 V and below. This new peak has been identified as P2′ with an orthorhombic crystal structure (see the dotted circles in **Figure 6c, 6f**), which is a distorted form of P2 phase (hexagonal structure). This is usually observed for Mn-rich compounds owing to their higher Mn^{3+} content in deep-discharged state and can be referred to the Jahn-Teller distortion. According to the previous research on P2-type Mn-based layered oxide materials for SIBs, this orthorhombic distorted phase was strongly influenced by the redox reaction of Mn during cell cycling and resulted in transition metal degradation/dissolution.[11,38] It was understood that the occurrence of P2-P2′ phase transition (bi-phasic region) and electrolyte decomposition (discussed in the latter section) were mainly responsible for the inferior electrochemical performance as well as the larger cell impedance in PVDF electrode. Nevertheless, the insufficient surface coverage due to the formation of cracks and cavities could be a possible reason for the phase transition observed in CMC electrode. In contrast, SMS based electrode did not show any P2′ transformation in the deep-discharge state (see **Figure 6i**).

Furthermore, XPS measurements on cycled electrodes validated the surface protection provided by SMS binder, which kept signals on the cycled electrode surface. The XPS profiles of PVDF-C *1s* / F *1s*, CMC-C *1s*, and SMS-Si *2p* areas acquired from pristine and cycled electrodes are shown in **Figure 7**. The presence of electrolyte degradation on PVDF-based electrodes is demonstrated by a significant peak at 684 eV in the PVDF-F *1s* spectra (**Figure 7b**), which is attributed to a metal-fluoride bond (MnF2 or NaF, for example). Meanwhile, after 200 cycles, the corresponding -CF2- and -CH2- bonds detected in the PVDF-C *1s* and F *1s* spectrums

(**Figure 7a, 7b**) disappeared. These findings point to the loss of PVDF binder on the electrode surface and explain why the electrochemical performance of PVDF-based electrodes has worsened during cell cycling. Similar behavior was seen with a CMC-based electrode, where peak intensities for related bonds (C=O, C-O-C, C-O, and C-C) in CMC- C *1s* spectra were dramatically lowered after cycling, as shown in **Figure 7c**, coupled with changes in peak position. This indicates that the surface environment is changing as well as the incidence of binder degradation on the electrode surface. In contrast, the peak location and intensity for the Si_{SMS} bond in the Si *2p* spectra (Figure 8d) were well maintained after cycling for SMS-based electrodes, despite the generation of Si-F byproducts at 104 eV.

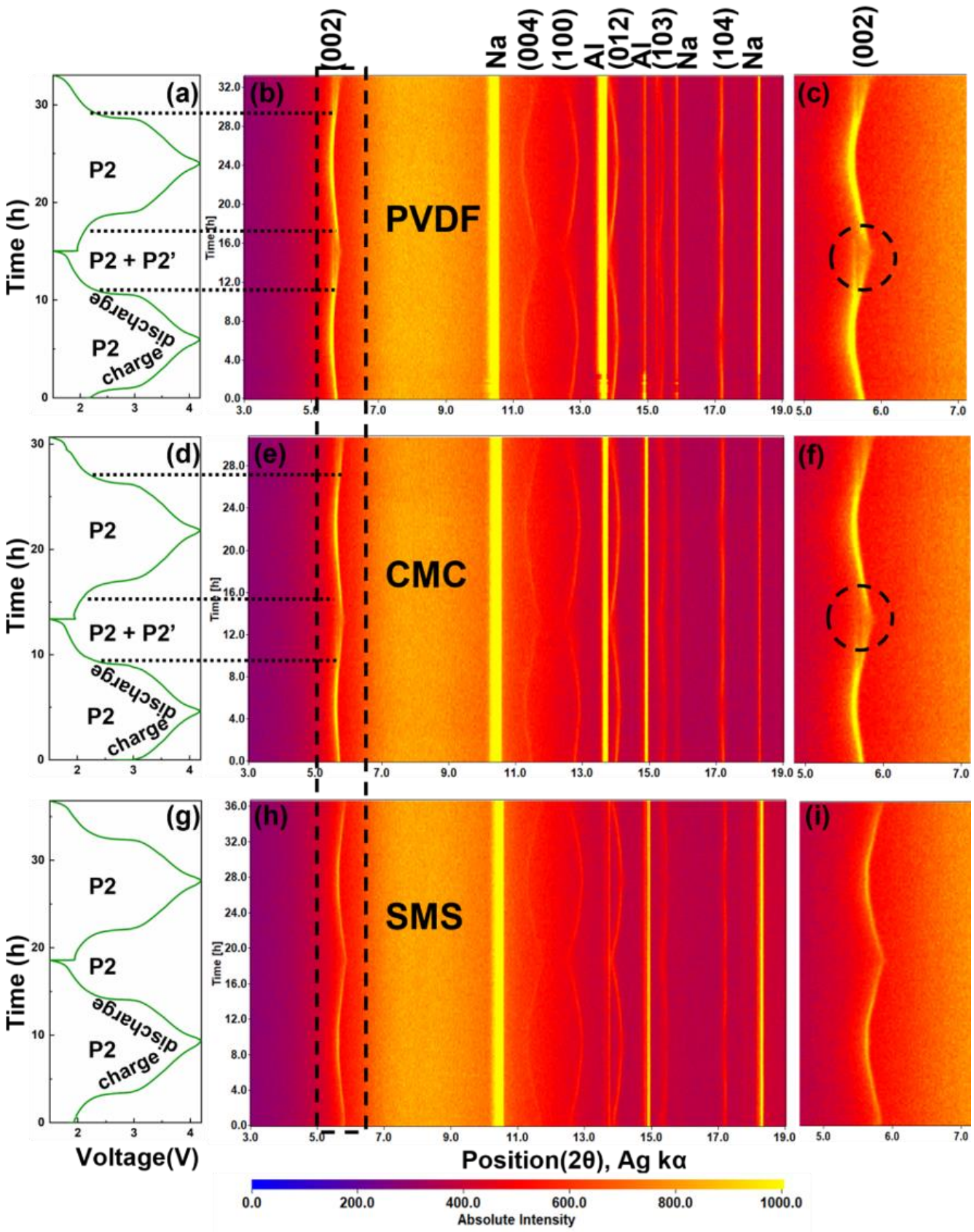
(a)
(b)
(c)
(d)
(e)
(f)
(g)
(h)
(i)
P2
P2 + P2'
P2
charge
discharge
Time (h)
Time [h]
PVDF
CMC
SMS
(002)
Na
(004)
(100)
Al
(012)
Al
(103)
Na
(104)
Na
(002)
Voltage(V)
Position(2θ), Ag kα
Absolute Intensity
0.0
200.0
400.0
600.0
800.0
1000.0

Figure 6. *Operando XRD analysis of NMNFT-PVDF, CMC and SMS electrodes during the initial two charge-discharge cycles in the potential window of 4.2–1.5 V at 0.1C rate. (a,d,g) charge-discharge profiles; (b,e,h) Operando XRD contour plots in the 2θ range of 3–19°; (c,f,i) enlarged view of (002) diffraction peak.*

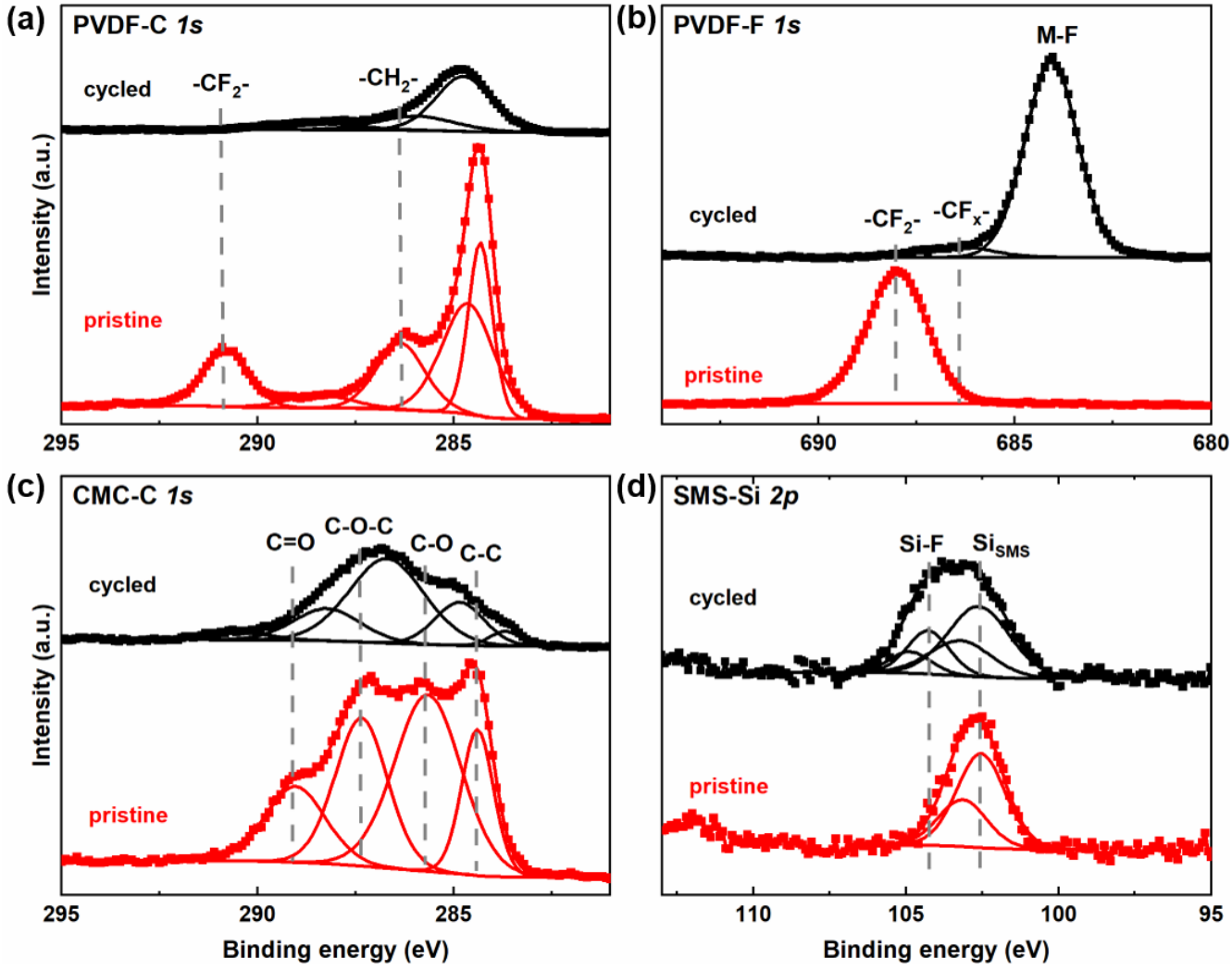

Figure 1. XPS profiles of (a) PVDF-C 1s, (b) PVDF-F 1s, (c) CMC-C 1s and (d) SMS-Si 2p regions recorded from different binder based pristine and cycled electrodes (200 cycles at a rate of 1C within the voltage window of 4.2–1.5 V)

Figure 8 displays the TEM images and EDS mappings of the cycled NMNFT-SMS electrode. As expected, owing to the surface coverage of SMS binder, no noticeable exfoliation or cracking of particles was observed after 200 cycles at 1C (see **Figure 8a, 8b).** EDS mappings as well as the corresponding spectra from **Figure S12** also confirm the uniform distribution of Na, Mn, Ti, Fe, C and O elements. It's worth mentioning that SMS surface coverage on cathode particles was well maintained after cycling (**Figure 8c**). In contrast, serious particle exfoliation/cracking problems have been reported by Zhou et al for uncoated P2-NMNO-PVDF electrodes.[38] With

Al_2O_3 as surface modification, the coated electrode showed a superior cycling performance without any defect.[38] In another study, ionic conductive Na_2SiO_3 coating and Si doping collaborative strategy was used to significantly improve the rate and cycling performance of P2-$Na_{0.67}Fe_{0.5}Mn_{0.5}O_2$ cathode material.[18]

Considering these results, SMS is confirmed to act not only as a binder for electrode preparation but also forms an *in-situ* surface coating on the cathode and carbon particles. This can effectively protect the active material surface from electrolyte attack and suppress the particle exfoliation/cracking during cycling, which enables improved electrochemical performance. The SMS binder is believed to form highly distributed and interconnected electronic/ionic percolation network, mitigate/suppress the volume changes caused by phase transformations, reduce parasitic reactions, and improves the reversibility of the process, which eventually leads to higher capacity retention.

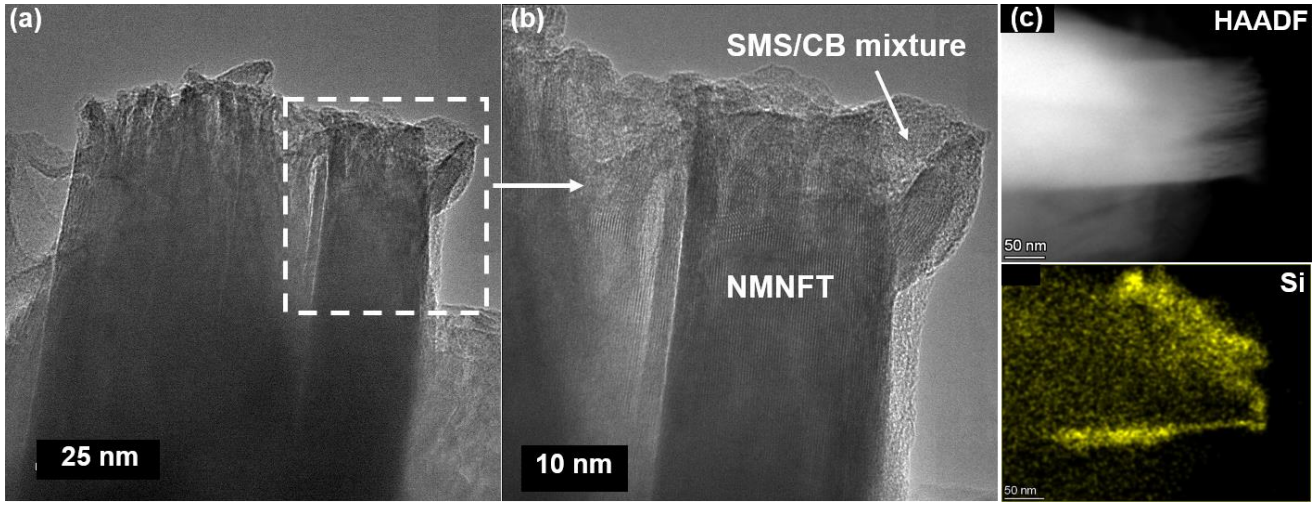

Figure 8. *TEM analysis of NMNFT-SMS-C cycled electrode. (a) Bright-field TEM image; (b) enlarged view of the selected area in (a); (c) HAADF image and STEM-EDS mappings Si signal.*

Thermal stability evaluation

Aside from electrochemical performance, thermal stability of the cathode material is an important issue to consider in total battery performance. The thermogravimetry analysis (TGA) coupled with differential scanning calorimetry (DSC) measurements on the different charged binder electrodes were performed to explore the favorable effect of different binders on electrode thermal stability. The TGA and DSC profiles of the charged electrodes are shown in **Figure 9** in comparison to the pristine cathode material. Among them, the charged SMS-based electrode had the best thermal stability, with just 7.1% weight loss after heating from 30 °C to 550 °C (see

Figure 9a). Meanwhile, weight losses of 16.2% and 19.0% were observed for charged CMC and PVDF-based electrodes, respectively. Pristine NMNFT powder exhibited a weight loss of only 1.4%.

The DSC profiles in **Figure 9b** demonstrate that the charged PVDF-based electrode displayed an endothermic event beginning about 100 °C and two exothermic heat release peaks at 390 °C and 469 °C, for a total exothermic heat release of 442.96 J/g (area under the curve-highlighted region). In contrast, the charged CMC and SMS electrodes showed a minor exothermic peak at 393 and 410 °C, with much lower heat releases of 111.78 J/g and 113.15 J/g, respectively. This demonstrates the better thermal stability of CMC and SMS electrodes. Furthermore, due to its uniform surface coverage on cathode particles and substantially higher decomposition temperature (>1000 °C), SMS is thought to operate as a heat shield or physical barrier. [30] SMS binders degrade at higher temperatures (or later) than PVDF and CMC binders under external heat, thereby insulating the cathode particle from heat and resulting in much lesser heat loss from the cathode via oxygen release. This could potentially reduce thermal runaway reactions and boost battery safety. **Table S9** shows the results acquired from the DSC curves under various settings.

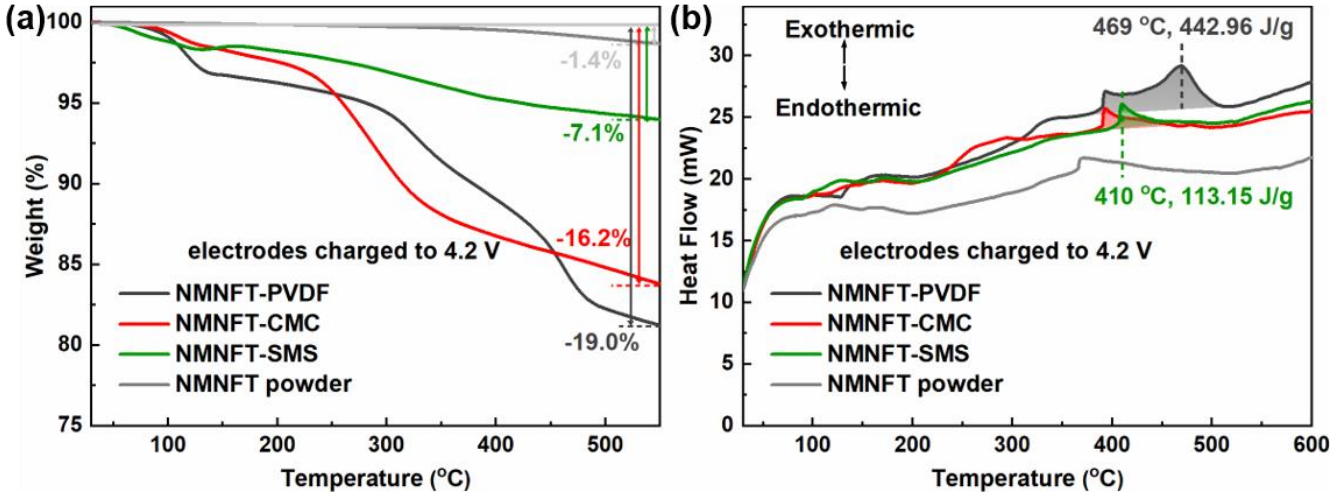

Figure 9. (a) TGA and (b) DSC profiles recorded from the charged electrodes and pristine cathode powder. Electrode composition - cathode: binder: carbon = 80:10:10.

Conclusions

In this study, P2-$Na_{0.67}Mn_{0.55}Ni_{0.25}Fe_{0.1}Ti_{0.1}O_2$ (NMNFT) cathode was successfully synthesized by a solid-state method, and the average oxidation state of transition metals in the bulk and surface was determined through XANES and XPS studies. The as-prepared NMNFT cathode demonstrated excellent chemical stability when exposed to air and water. Following that, the favorable impacts of aqueous binders on electrochemical performance and thermal stability were studied. When compared to the well-known CMC and PVDF binders, the

NMNFT-SMS electrode demonstrated superior electrochemical and thermal performances, which could be attributed to the formation of amorphous surface layers on the cathode and carbon particles, as well as the strong binding ability and high thermal stability provided by the SMS binder itself. According to the results of the Operando XRD, TEM, and XPS tests, the SMS binder effectively shielded the active material from electrolyte attack and particle exfoliation/cracking, as well as suppressed/delayed the P2 phase transformation, providing better electrochemical performance. Overall, sodium metasilicate (SMS) has the potential to be a multifunctional binder for this system, improving both electrochemical performance and safety. Furthermore, it has the potential to make positive electrode manufacturing less expensive, safer, and more sustainable.

Acknowledgements

This work contributes to the research performed at CELEST (Center for Electrochemical Energy Storage Ulm-Karlsruhe) and was funded by the German Research Foundation (DFG) under project ID 390874152 (POLiS Cluster of Excellence, EXC 2154). PB is grateful to the Alexander von Humboldt Foundation (Bonn, Germany) for a 2022 Humboldt fellowship for experienced researchers. This project received funding from the European Union's Horizon 2020 research and innovation program under grant agreement No 957189. The authors acknowledge BATTERY 2030PLUS funded by the European Union's Horizon 2020 research and innovation program under Grant Agreement No. 957213.

Author Contributions

Conceptualization: VP, Methodology: RX and VP, Investigation: RX, VP, YT, SF, HS, BD, ZK, SB, YH, ST, Validation: VP and RX, Formal Analysis: VP and RX, Resources: MF, Writing – Original Draft: RX and VP, Visualization: VP, Writing – Review & Editing: MAR, PB and MF, Supervision: VP, Project Administration: MF, Funding Acquisition: MF.

References

[1] K. Kubota, S. Komaba, *J. Electrochem. Soc.* **2015**, *162*, A2538.
[2] J. F. Peters, A. Peña Cruz, M. Weil, *Batteries* **2019**, *5*, 10.
[3] N. Tapia-Ruiz, A. R. Armstrong, H. Alptekin, M. A. Amores, H. Au, J. Barker, R. Boston, W. R. Brant, J. M. Brittain, Y. Chen, M. Chhowalla, Y.-S. Choi, S. I. R. Costa, M. C. Ribadeneyra, S. A. Cussen, E. J. Cussen, W. I. F. David, A. V. Desai, S. A. M. Dickson, E. I. Eweka, J. D. Forero-Saboya, C. P. Grey, J. M. Griffin, P. Gross, X. Hua, J. T. S. Irvine, P. Johansson, M. O. Jones, M. Karlsmo, E. Kendrick, E. Kim, O. V. Kolosov, Z. Li, S. F. L. Mertens, R. Mogensen, L. Monconduit, R. E. Morris, A. J. Naylor, S. Nikman, C. A. O'Keefe, D. M. C. Ould, R. G. Palgrave, P. Poizot, A. Ponrouch, S. Renault, E. M. Reynolds, A. Rudola, R. Sayers, D. O. Scanlon, S. Sen, V. R. Seymour, B.

Silván, M. T. Sougrati, L. Stievano, G. S. Stone, C. I. Thomas, M.-M. Titirici, J. Tong, T. J. Wood, D. S. Wright, R. Younesi, *J. Phys. Energy* **2021**, *3*, 031503.
[4] C. Delmas, *Advanced Energy Materials* **2018**, *8*, 1703137.
[5] C. Delmas, C. Fouassier, P. Hagenmuller, *Physica B+C* **1980**, *99*, 81–85.
[6] T. Song, E. Kendrick, *J. Phys. Mater.* **2021**, *4*, 032004.
[7] K. Kubota, N. Yabuuchi, H. Yoshida, M. Dahbi, S. Komaba, *MRS Bulletin* **2014**, *39*, 416–422.
[8] Y. Mo, S. P. Ong, G. Ceder, *Chem. Mater.* **2014**, *26*, 5208–5214.
[9] S. Guo, Y. Sun, J. Yi, K. Zhu, P. Liu, Y. Zhu, G. Zhu, M. Chen, M. Ishida, H. Zhou, *NPG Asia Mater* **2016**, *8*, e266–e266.
[10] Z. Lu, J. R. Dahn, *J. Electrochem. Soc.* **2001**, *148*, A1225.
[11] Q. Liu, Z. Hu, M. Chen, C. Zou, H. Jin, S. Wang, Q. Gu, S. Chou, *J. Mater. Chem. A* **2019**, *7*, 9215–9221.
[12] K. Wang, Z.-G. Wu, G. Melinte, Z.-G. Yang, A. Sarkar, W. Hua, X. Mu, Z.-W. Yin, J.-T. Li, X.-D. Guo, B.-H. Zhong, C. Kübel, *Journal of Materials Chemistry A* **2021**, *9*, 13151–13160.
[13] M. H. Han, N. Sharma, E. Gonzalo, J. C. Pramudita, H. E. A. Brand, J. M. L. del Amo, T. Rojo, *Journal of Materials Chemistry A* **2016**, *4*, 18963–18975.
[14] C. Zhang, R. Gao, L. Zheng, Y. Hao, X. Liu, *ACS Appl. Mater. Interfaces* **2018**, *10*, 10819–10827.
[15] S. Tao, W. Zhou, D. Wu, Z. Wang, B. Qian, W. Chu, A. Marcelli, L. Song, *Journal of Materials Science & Technology* **2021**, *74*, 230–236.
[16] R. J. Clément, Z. Lun, G. Ceder, *Energy Environ. Sci.* **2020**, *13*, 345–373.
[17] W. Zuo, J. Qiu, X. Liu, F. Ren, H. Liu, H. He, C. Luo, J. Li, G. F. Ortiz, H. Duan, J. Liu, M.-S. Wang, Y. Li, R. Fu, Y. Yang, *Nat Commun* **2020**, *11*, 3544.
[18] J. Jiao, K. Wu, R. Dang, N. Li, X. Deng, X. Liu, Z. Hu, X. Xiao, *Electrochimica Acta* **2021**, *384*, 138362.
[19] S.-L. Chou, Y. Pan, J.-Z. Wang, H.-K. Liu, S.-X. Dou, *Phys. Chem. Chem. Phys.* **2014**, *16*, 20347–20359.
[20] D. Bresser, D. Buchholz, A. Moretti, A. Varzi, S. Passerini, *Energy Environ. Sci.* **2018**, *11*, 3096–3127.
[21] R. Wang, L. Feng, W. Yang, Y. Zhang, Y. Zhang, W. Bai, B. Liu, W. Zhang, Y. Chuan, Z. Zheng, H. Guan, *Nanoscale Res Lett* **2017**, *12*, 575.
[22] Y. Liu, R. Zhang, J. Wang, Y. Wang, *iScience* **2021**, *24*, 102332.
[23] J. Zhao, X. Yang, Y. Yao, Y. Gao, Y. Sui, B. Zou, H. Ehrenberg, G. Chen, F. Du, *Adv. Sci.* **2018**, *5*, 1700768.
[24] J. Ming, H. Ming, W.-J. Kwak, C. Shin, J. Zheng, Y.-K. Sun, *Chemical Communications* **2014**, *50*, 13307–13310.
[25] N. Loeffler, G.-T. Kim, F. Mueller, T. Diemant, J.-K. Kim, R. J. Behm, S. Passerini, *ChemSusChem* **2016**, *9*, 1112–1117.
[26] C. Marino, E. Marelli, S. Park, C. Villevieille, *Batteries* **2018**, *4*, 66.
[27] F. Jeschull, D. Brandell, M. Wohlfahrt-Mehrens, M. Memm, *Energy Technology* **2017**, *5*, 2108–2118.
[28] C.-C. Li, J.-T. Lee, Y.-L. Tung, C.-R. Yang, *J Mater Sci* **2007**, *42*, 5773–5777.
[29] S. Trivedi, V. Pamidi, M. Fichtner, M. A. Reddy, *Green Chemistry* **2022**, *24*, 5620–5631.
[30] S. Trivedi, S. Dinda, Y. Tang, S. Fuchs, V. Pamidi, H. S. Stein, A. R. Munnangi, M. Fichtner, *Journal of Energy Storage* **2023**, *73*, 109210.
[31] S. Trivedi, V. Pamidi, S. P. Bautista, F. N. A. Shamsudin, M. Weil, P. Barpanda, D. Bresser, M. Fichtner, *Advanced Energy Materials* **n.d.**, *n/a*, 2303338.
[32] C. Wei, M. N. Obrovac, *J. Electrochem. Soc.* **2021**, *168*, 020505.
[33] J. Rodríguez-Carvajal, *Physica B: Condensed Matter* **1993**, *192*, 55–69.
[34] N. Fairley, V. Fernandez, M. Richard-Plouet, C. Guillot-Deudon, J. Walton, E. Smith, D. Flahaut, M. Greiner, M. Biesinger, S. Tougaard, D. Morgan, J. Baltrusaitis, *Applied Surface Science Advances* **2021**, *5*, 100112.
[35] M. Anji Reddy, M. Helen, A. Groß, M. Fichtner, H. Euchner, *ACS Energy Lett.* **2018**, *3*, 2851–2857.
[36] R.-R. Li, Z. Yang, X.-X. He, X.-H. Liu, H. Zhang, Y. Gao, Y. Qiao, L. Li, S.-L. Chou, *Chem. Commun.* **2021**, *57*, 12406–12416.
[37] S. Doubaji, B. Philippe, I. Saadoune, M. Gorgoi, T. Gustafsson, A. Solhy, M. Valvo, H. Rensmo, K. Edström, *ChemSusChem* **2016**, *9*, 97–108.
[38] Y. Yoda, K. Kubota, H. Isozumi, T. Horiba, S. Komaba, *ACS Appl. Mater. Interfaces* **2018**, *10*, 10986–10997.
[39] M. Kuenzel, D. Bresser, T. Diemant, D. V. Carvalho, G.-T. Kim, R. J. Behm, S. Passerini, *ChemSusChem* **2018**, *11*, 562–573.
[40] Y. Liu, X. Fang, A. Zhang, C. Shen, Q. Liu, H. A. Enaya, C. Zhou, *Nano Energy* **2016**, *27*, 27–34.
[41] L. Ling, Y. Bai, Z. Wang, Q. Ni, G. Chen, Z. Zhou, C. Wu, *ACS Appl. Mater. Interfaces* **2018**, *10*, 5560–5568.

[42] H. Xu, K. Jiang, X. Zhang, X. Zhang, S. Guo, H. Zhou, *ACS Appl. Mater. Interfaces* **2019**, *11*, 26817–26823.
[43] Q.-C. Zhuang, X.-Y. Qiu, S.-D. Xu, Y.-H. Qiang, S.-G. Sun, Q.-C. Zhuang, X.-Y. Qiu, S.-D. Xu, Y.-H. Qiang, S.-G. Sun, in *Lithium Ion Batteries - New Developments*, IntechOpen, **2012**.
[44] I. Yamada, Y. Iriyama, T. Abe, Z. Ogumi, *Journal of Power Sources* **2007**, *172*, 933–937.
[45] X. Wang, H. Hao, J. Liu, T. Huang, A. Yu, *Electrochimica Acta* **2011**, *56*, 4065–4069.
[46] W. Weppner, R. A. Huggins, *J. Electrochem. Soc.* **1977**, *124*, 1569.